# Parameter Design and Convergence Analysis of Flux Observer for Sensorless PMSM Drives

Mingming Zhang [ID], Binyu Xia [ID], and Jun Zhang [ID]

*Abstract*—**Position observer design is one of the most important tasks for sensorless PMSM drives. In this paper, we apply extended state observer (ESO) to estimate the PMSM angular position. For the operation of constant velocity, we use the linearization technique to study the error dynamics and design parameter tuning strategies for fast convergence and robustness against adverse effects. We further analyze the equilibria distributions of the estimation error dynamics and ensure that the origin is the only stable equilibrium. For velocity tracking, the ESO estimator can be readily extended to deal with this case and its global convergence is guaranteed by the results of slowly varying systems. The experimental results on a 750 W motor drive demonstrate the efficacy of the ESO position observer.**

*Index Terms*—**Equilibria analysis, global convergence, sensorless PMSM drives, parameter tuning, position estimation.**

## I. INTRODUCTION

**P**ERMANENT Magnet Synchronous Motor (PMSM) is used in many aspects of the modern industry due to its high power density, high energy efficiency, and prompt dynamic response [1], [2]. The dynamics of motor drives in the three-phase stationary frame is nonlinear, and researchers developed field oriented control (FOC) to convert it into a linear system in a two-phase rotationary frame.

To take advantage of FOC, we need to know the rotor angular position. One crucial objective is to get the rotor angular position in the widest possible speed range. In recent years, the sensorless technique is employed in many applications where the position is estimated from the underlying physics of the motor, and it attracts extensive research interests owing to its lower cost and maintenance, less cabling, and increased fault tolerance [3], [4].

Over the years, researchers and engineers have developed many effective position observers. One common method is to estimate rotor position from the back electro motive force (EMF) signal, including Sliding Mode Observer [5]–[7], Luenberger State Observer [8], [9], and Extended Kalman Filter [10], [11].

Because the back-EMF signal is proportional to the rotor speed, these observers are not applicable in the low speed range. To estimate the rotor position from standstill to low speed, researchers use the saliency of the Interior PM (IPM) and developed High Frequency signal Injection (HFI) method [12]–[14]. However, the HFI method is not applicable for non-salient PMSMs and may generate acoustic noises and mechanical vibrations. Furthermore, to address the crucial requirement on the observer convergence as in any observer, [15], [16] developed Higher Order observer, even though it usually demands considerable computational resources and the tuning of design parameters can be complicated.

Another type of position observer is to use the magnetic flux of PMSM. Some early works include the Voltage Model (VM) [17], [18] that calculate the rotor position from stator flux linkage. Harnefors *et al.* [19] improves the estimation performance in the low speed range and the synchronization of rotor position provided that the stator resistance is underestimated. In recent years, a flux-based adaptive full-order observer [20], [21] is successfully applied in many industrial applications, which has accurate estimation performance, and can overcome the instability problem caused by the fixed feedback gain design in VM. Local behavior of the adaptive full-order observer about a specified operating point is studied thoroughly in [22], where the origin is assumed the only equilibrium of the error dynamics by default. Further, parameter adaptation laws are combined with the flux-based observer in [23]–[25].

In the past several decades, extended state observer (ESO) method has made tremendous success in numerous industrial applications [26]–[29]. ESO requires only basic knowledge of the plant model, and it can achieve accurate estimation with fast and robust convergence. These advantages make ESO a promising candidate for position sensorless control in PMSM drives. In this paper, we apply ESO method to estimate the PMSM flux and the desired angular position.

The key contributions of this paper are as follows:
1) We proposed a nonlinear position observer to achieve fast convergence and noise suppression. A linear version is also given for implementation ease, which turns out to be equivalent to the adaptive full-order observer in [21].
2) We proved that the proposed position observer is globally convergent by using the results from slowly varying systems. To our best knowledge, this theoretical result on global convergence is the first of the kind in the literature. Moreover, this proof can be readily extended to the other flux-based observers previously investigated (e.g. in [21]),

which thus provides a needed feature for the existing observers.

3) We performed a thorough investigation on the equilibria distribution of the estimation error dynamics. This analysis enables us to guarantee that the origin is the only stable equilibrium and thus to obtain an unbiased estimation.

4) We developed an optimal gain design to fight against the inevitable model parameter deviations and uncertainties based on sensitivity analysis. We demonstrated this feature experimentally to show that the proposed position observer is more robust against these adverse effects.

All these results are corroborated experimentally with a 750 W PMSM, as shown in Section VI.

## II. BACKGROUND

In this section, we introduce basic background for the mathematical model of PMSM. To make this paper self-contained, we include some basic knowledge reported in [20]–[22], and we acknowledge their contributions in this field.

### A. PMSM Model in the Real dq Frame

Denote the variables in $dq$-frame with the subscript $s$. The voltage equation of PMSM in $dq$-frame can be written as

$$\frac{d}{dt}\boldsymbol{\psi}_s = \boldsymbol{u}_s - R_s \boldsymbol{i}_s - \omega \boldsymbol{J} \boldsymbol{\psi}_s, \tag{1}$$

where $\theta$ is the electrical angular position, $\boldsymbol{\psi}_s = [\psi_{sd}, \psi_{sq}]^T$ the stator flux, $\boldsymbol{u}_s = [u_{sd}, u_{sq}]^T$ the stator voltage, $\boldsymbol{i}_s = [i_{sd}, i_{sq}]^T$ the stator current, $R_s$ the stator resistance, $\omega$ the electrical angular velocity, and $\boldsymbol{J} = \begin{bmatrix} 0 & -1 \\ 1 & 0 \end{bmatrix}$. The stator flux linkage is given by

$$\boldsymbol{\psi}_s = \underbrace{\begin{bmatrix} L_d & 0 \\ 0 & L_q \end{bmatrix}}_{\boldsymbol{L}} \boldsymbol{i}_s + \underbrace{\begin{bmatrix} \psi_f \\ 0 \end{bmatrix}}_{\boldsymbol{\psi}_f}, \tag{2}$$

where $L_d$ is the $d$-axis inductance, $L_q$ the $q$-axis inductance, $\boldsymbol{L}$ the inductance matrix, and $\boldsymbol{\psi}_f$ the permanent-flux linkage vector. Note that the inductance matrix $\boldsymbol{L}$ can vary due to magnetic saturation and cross saturation effects [30]. In this paper, we use constant inductance parameters for simplicity.

### B. PMSM Model in the Estimator Frame

Denote the estimated angular position as $\hat{\theta}$, and the estimation error as $\tilde{\theta} = \theta - \hat{\theta}$. The estimator frame can then be defined as its direct axis being aligned with $\hat{\theta}$ and denoted as $\hat{d}$.

Denote the variables in the estimator frame with no subscript. Now the transformation from the real frame to the estimator frame is a counterclockwise rotation by $\tilde{\theta}$:

$$\boldsymbol{\psi} = e^{\tilde{\theta}\boldsymbol{J}}\boldsymbol{\psi}_s, \quad \boldsymbol{i} = e^{\tilde{\theta}\boldsymbol{J}}\boldsymbol{i}_s, \quad \boldsymbol{u} = e^{\tilde{\theta}\boldsymbol{J}}\boldsymbol{u}_s, \tag{3}$$

where $e^{\tilde{\theta}\boldsymbol{J}} = \cos\tilde{\theta}\boldsymbol{I} + \sin\tilde{\theta}\boldsymbol{J}$ is the matrix exponential function, and $\boldsymbol{I}$ is the identity matrix.

Substituting (3) into (1) and after some algebraic derivations, we can obtain the mathematical model of PMSM as

$$\frac{d}{dt}\boldsymbol{\psi} = \boldsymbol{u} - R_s\boldsymbol{i} - \hat{\omega}\boldsymbol{J}\boldsymbol{\psi}, \tag{4}$$

where $\hat{\omega}$ is the estimated electrical angular velocity. Hereafter we use the symbol $\hat{\ }$ to represent the estimated variable, and the symbol $\tilde{\ }$ to represent the estimation error. In contrast to (2), the stator flux linkage in the estimator frame is now dependent on the estimation error $\tilde{\theta}$:

$$\boldsymbol{\psi} = e^{\tilde{\theta}\boldsymbol{J}}\boldsymbol{L}e^{-\tilde{\theta}\boldsymbol{J}}\boldsymbol{i} + e^{\tilde{\theta}\boldsymbol{J}}\boldsymbol{\psi}_f. \tag{5}$$

### C. Linearization of the PMSM Model

Note that the PMSM model in the estimator frame (4) is nonlinear because it contains the term $\hat{\omega}\boldsymbol{J}\boldsymbol{\psi}$. In general, a nonlinear system is difficult to analyze and design. An effective way is to linearize this model around an operating point $O = (\boldsymbol{\psi}_0, \tilde{\theta}_0, \omega_0)$, at which the dynamics vanishes. For the ideal case when the steady-state position estimation error is 0, *i.e.*, $\tilde{\theta}_0 = 0$, the linearized model of PMSM at the operating point is obtained as

$$\frac{d}{dt}\delta\boldsymbol{\psi} = -(R_s\boldsymbol{L}^{-1} + \omega_0\boldsymbol{J})\delta\boldsymbol{\psi} - \boldsymbol{J}\boldsymbol{\psi}_0\delta\omega + \delta\boldsymbol{u}$$
$$+ (R_s\boldsymbol{L}^{-1}\boldsymbol{J}\boldsymbol{\psi}_{a0}\delta\tilde{\theta} + \boldsymbol{J}\boldsymbol{\psi}_0\delta\tilde{\omega}),$$
$$\frac{d}{dt}\delta\theta = \delta\omega,$$
$$\frac{d}{dt}\delta\theta = \frac{d}{dt}\delta\omega = h_\delta. \tag{6}$$

with

$$\boldsymbol{\psi}_{a0} = \begin{bmatrix} \psi_{ad0} \\ \psi_{aq0} \end{bmatrix} = \begin{bmatrix} (L_d - L_q)i_{d0} + \psi_f \\ -(L_d - L_q)i_{q0} \end{bmatrix}. \tag{7}$$

Eq. (7) is the auxiliary-flux defined in [21]. Note that to be consistent with the standard ESO formulation, we include the dynamics of $\delta\omega$ in (6), in which case $h_\delta$ represents the mechanical dynamics.

## III. ANGULAR POSITION OBSERVER FOR FIXED VELOCITY

In this section, we apply the nonlinear extended state observer (ESO) method to design a position observer and discuss its parameter tuning strategy.

### A. Angular Position Observer Design

The basic idea of observer design is to use the difference between the measured output and the estimated one as an error signal to drive the observer with the objective that this error will go to 0. Here we form the error signal from the difference between $\boldsymbol{i}$ and its estimation $\hat{\boldsymbol{i}}$ as common.

It is well-known that in a PMSM the time scales for the electromagnetic and mechanical parts can differ by several orders. In general, voltage, current, and flux can achieve steady states in the regime of microsecond, whereas the dynamics of angular speed is much slower due to the mechanical inertia. In the electromagnetic time scale, the dynamical term $h_\delta$ in (6)

is small and bounded, which satisfies the requirement of the extended state in ESO as discussed in [31], [32].

Note that the term $R_s \boldsymbol{L}^{-1} \boldsymbol{J} \psi_{a0} \delta\tilde{\theta} + \boldsymbol{J}\psi_0 \delta\tilde{\omega}$ in the second line of (6) comes from the difference between the estimator and real frame, and it vanishes if the estimation error converges to 0. We now take $\delta\omega$ as the extended state and design the ESO for the linearized system model (6) as

$$\frac{d}{dt}\delta\hat{\psi} = -(R_s \boldsymbol{L}^{-1} + \omega_0 \boldsymbol{J})\delta\hat{\psi} - \boldsymbol{J}\psi_0 \delta\hat{\omega} + \delta\boldsymbol{u} + \boldsymbol{G}_1 \operatorname{fal}(\delta\boldsymbol{e}),$$

$$\frac{d}{dt}\delta\hat{\theta} = \delta\hat{\omega} + \boldsymbol{g}_2 \operatorname{fal}(\delta\boldsymbol{e}),$$

$$\frac{d}{dt}\delta\hat{\omega} = \boldsymbol{g}_3 \operatorname{fal}(\delta\boldsymbol{e}),$$

$$\delta\boldsymbol{e} = \boldsymbol{L}\delta\tilde{\boldsymbol{i}}, \quad \delta\hat{\boldsymbol{i}} = \boldsymbol{L}^{-1}\delta\hat{\psi}, \tag{8}$$

where $\boldsymbol{G}_1 \in \mathbb{R}^{2\times 2}$, $\boldsymbol{g}_2$ and $\boldsymbol{g}_3 \in \mathbb{R}^{1\times 2}$ are the feedback gains. The nonlinear function fal is defined by

$$\operatorname{fal}(e) = \begin{cases} \dfrac{e}{\eta^{a-1}}, & |e| \leq \eta, \\[2mm] |e|^a \operatorname{sign}(e), & |e| > \eta. \end{cases} \tag{9}$$

Choosing small $\eta > 0$ and $0 < a < 1$ in fal can accelerate the settling procedure and help reduce the steady-state error [33].

From the observer design (8) for the linearized model, following the standard procedure in [34], we can extend it for the original nonlinear model (4) as

$$\frac{d}{dt}\hat{\psi} = \boldsymbol{u} - R_s\boldsymbol{i} - \hat{\omega}\boldsymbol{J}\hat{\psi} + \boldsymbol{G}_1 \operatorname{fal}(\boldsymbol{e}), \tag{10a}$$

$$\frac{d}{dt}\hat{\theta} = \hat{\omega} + \boldsymbol{g}_2 \operatorname{fal}(\boldsymbol{e}), \tag{10b}$$

$$\frac{d}{dt}\hat{\omega} = \boldsymbol{g}_3 \operatorname{fal}(\boldsymbol{e}), \tag{10c}$$

$$\boldsymbol{e} = \boldsymbol{L}(\boldsymbol{i} - \hat{\boldsymbol{i}}) = \boldsymbol{L}\tilde{\boldsymbol{i}}, \tag{10d}$$

$$\hat{\boldsymbol{i}} = \boldsymbol{L}^{-1}(\hat{\psi} - \psi_f). \tag{10e}$$

If replacing the nonlinear feedback terms $\operatorname{fal}(\boldsymbol{e})$ in (10) by the linear feedback terms $\boldsymbol{e}$, we can obtain a linear version of ESO (LESO), which is mathematically equivalent to the adaptive full-order observer proposed in [21].

### B. Error Dynamics Analysis

Hereby we derive the estimation error dynamics. We firstly consider the case when a motor is running at a constant velocity $\omega_0$. The dynamics of the flux estimation error can be obtained by subtracting (10) from (4):

$$\frac{d}{dt}\tilde{\psi} = -(\omega_0 - \tilde{\omega})\boldsymbol{J}\tilde{\psi} - \boldsymbol{G}_1 \operatorname{fal}(\boldsymbol{e}),$$

$$\frac{d}{dt}\tilde{\theta} = \tilde{\omega} - \boldsymbol{g}_2 \operatorname{fal}(\boldsymbol{e}),$$

$$\frac{d}{dt}\tilde{\omega} = -\boldsymbol{g}_3 \operatorname{fal}(\boldsymbol{e}). \tag{11}$$

Because (11) is a nonlinear differential equation, we again use the linearization technique to analyze its dynamics. Note that the different choices of gain matrices affect not only the error dynamics but also the system equilibria, that is the steady-state estimation error. We want the system (11) to converge to equilibrium with no estimation error, and the nonzero equilibria will be discussed in Section IV. Denote the state variable of the complete estimation error dynamics in (11) as $\boldsymbol{x} = [\tilde{\psi}, \tilde{\theta}, \tilde{\omega}]^T$, the desired equilibrium state with no estimation error as

$$\boldsymbol{x}_0^* = [\boldsymbol{0}, \ 0, \ 0]^T, \tag{12}$$

and the deviation around $\boldsymbol{x}_0^*$ is denoted as

$$\delta\boldsymbol{x} = \left[\delta\tilde{\psi}, \ \delta\tilde{\theta}, \ \delta\tilde{\omega}\right]^T. \tag{13}$$

Since the dynamics of $\delta\psi$ is given in (6) and that of $\delta\hat{\psi}$ in (8), we can readily obtain the dynamics of $\delta\tilde{\psi}$. Further, it is easy to derive the linearization of the function fal. Combining these two results, we can get the linearized estimation error dynamics around $\boldsymbol{x}_0^*$ as

$$\frac{d}{dt}\delta\boldsymbol{x} = A\,\delta\boldsymbol{x}, \tag{14}$$

where $A$ is a $4 \times 4$ matrix[1]:

$$A = \begin{bmatrix} -(\omega_0 \boldsymbol{J} + \boldsymbol{G}_1) & \boldsymbol{G}_1 \boldsymbol{J}\psi_{a0} & 0 \\ -\boldsymbol{g}_2 & \boldsymbol{g}_2 \boldsymbol{J}\psi_{a0} & 1 \\ -\boldsymbol{g}_3 & \boldsymbol{g}_3 \boldsymbol{J}\psi_{a0} & 0 \end{bmatrix}. \tag{15}$$

### C. Parameter Tuning

Moreover, we want to choose appropriate feedback gain matrices $\boldsymbol{G}_1, \boldsymbol{g}_2$, and $\boldsymbol{g}_3$ to ensure the estimation error convergence to 0 and to achieve other performance criteria such as robustness against model parameter uncertainties.

To simplify the design, we can decouple the dynamics of the flux from that of the speed by letting $\boldsymbol{G}_1 \boldsymbol{J}\psi_{a0} = 0$, which is in a similar fashion as [22]. This way the error dynamics of the flux is determined by the matrix $-(\omega_0 \boldsymbol{J} + \boldsymbol{G}_1)$, and that of the speed is determined by

$$\boldsymbol{T} \triangleq \begin{bmatrix} \boldsymbol{g}_2 \boldsymbol{J}\psi_{a0} & 1 \\ \boldsymbol{g}_3 \boldsymbol{J}\psi_{a0} & 0 \end{bmatrix}.$$

*1) Flux Estimation:* We can design $\boldsymbol{G}_1$ such that

$$\det(s\boldsymbol{I} + \omega_0 \boldsymbol{J} + \boldsymbol{G}_1) = s^2 + 2\zeta_1\omega_1 s + \omega_1^2, \tag{16}$$

where $\zeta_1$ and $\omega_1$ are the desired damping ratio and natural frequency respectively. By solving (16), we obtain

$$\boldsymbol{G}_1 = \left[2\zeta_1\omega_1 \boldsymbol{I} + (\omega_1^2/\omega_0 - \omega_0)\boldsymbol{J}\right] \frac{\psi_{a0}\psi_{a0}^T}{\|\psi_{a0}\|^2}. \tag{17}$$

The gain matrix $\boldsymbol{G}_1$ is equivalent to the gain matrix $\boldsymbol{K}$ in [21].

---

[1]Notice that there exist slight abuse of notations in (10) and (15): the $G_i$'s in these two equations differ by a factor of $\delta^{1-a}$.

*2) Speed/Position Estimation:* We can choose $\boldsymbol{g}_2$ and $\boldsymbol{g}_3$ such that

$$\det(s\boldsymbol{I} - \boldsymbol{T}) = s^2 + 2\zeta_2\omega_2 s + \omega_2^2, \tag{18}$$

where the damping ratio $\zeta_2$ and the natural frequency $\omega_2$ can be chosen appropriately according to the operating condition so as to achieve fast convergence. Equating the coefficients on both sides of (18), we have

$$\boldsymbol{g}_2\boldsymbol{J}\boldsymbol{\psi}_{a0} = -2\zeta_2\omega_2, \quad \boldsymbol{g}_3\boldsymbol{J}\boldsymbol{\psi}_{a0} = -\omega_2^2. \tag{19}$$

It is noted that we have 4 independent variables in the gain vectors $\boldsymbol{g}_2$ and $\boldsymbol{g}_3$ to satisfy 2 equations in (19). We can then make use of the extra 2 freedoms to improve the system robustness against model parameter uncertainties, especially the inductance variations.

To this end, we rewrite (19) as

$$\boldsymbol{G}\boldsymbol{v}_1 = \boldsymbol{v}_2, \tag{20}$$

where $\boldsymbol{G} = [\boldsymbol{g}_2, \boldsymbol{g}_3]^T$, $\boldsymbol{v}_1 = \boldsymbol{J}\boldsymbol{\psi}_{a0}$, $\boldsymbol{v}_2 = [-2\zeta_2\omega_2, -\omega_2^2]^T$. Suppose that the parameter uncertainties in $\boldsymbol{v}_1$ is $\delta\boldsymbol{v}_1$, and the resulting perturbation in $\boldsymbol{v}_2$ is $\delta\boldsymbol{v}_2$. Then,

$$\boldsymbol{G}(\boldsymbol{v}_1 + \delta\boldsymbol{v}_1) = \boldsymbol{v}_2 + \delta\boldsymbol{v}_2. \tag{21}$$

which yields that

$$\boldsymbol{G}\delta\boldsymbol{v}_1 = \delta\boldsymbol{v}_2. \tag{22}$$

It is desired to minimize the deviation $\delta\boldsymbol{v}_2$ such that the poles of the speed error dynamics stay close to the desired locations.

We know that

$$\|\delta\boldsymbol{v}_2\|_2 = \|\boldsymbol{G}\delta\boldsymbol{v}_1\|_2 \leq \|\boldsymbol{G}\|_{2,i}\|\delta\boldsymbol{v}_1\|_2, \tag{23}$$

where $\|\boldsymbol{G}\|_{2,i}$ is the induced 2-norm of $\boldsymbol{G}$ defined by $\|\boldsymbol{G}\|_{2,i} = \sup_{\boldsymbol{v}\neq\boldsymbol{0}}(\|\boldsymbol{G}\boldsymbol{v}\|_2/\|\boldsymbol{v}\|_2)$. From (23), we can minimize $\|\boldsymbol{G}\|_{2,i}$ to reduce the upper bound of $\|\delta\boldsymbol{v}_2\|_2$. This leads to the following optimization problem:

$$\begin{aligned} \text{minimize} \quad &\|\boldsymbol{G}\|_{2,i} \\ \text{subject to} \quad &\boldsymbol{G}\boldsymbol{v}_1 = \boldsymbol{v}_2. \end{aligned} \tag{24}$$

The optimal solution can be obtained as

$$\boldsymbol{g}_2 = 2\zeta_2\omega_2\frac{\boldsymbol{\psi}_{a0}^T\boldsymbol{J}}{\|\boldsymbol{\psi}_{a0}\|^2}, \quad \boldsymbol{g}_3 = \omega_2^2\frac{\boldsymbol{\psi}_{a0}^T\boldsymbol{J}}{\|\boldsymbol{\psi}_{a0}\|^2}. \tag{25}$$

Hereby we prove by construction to show that (25) is the optimal solution of (24). For brevity of notation, we drop the subscript 2 in the 2-norm in the following. From the definition of the induced 2-norm, it is obtained

$$\|\boldsymbol{G}\|_{2,i} \geq \|\boldsymbol{G}\boldsymbol{v}_1\|/\|\boldsymbol{v}_1\|. \tag{26}$$

According to (20), i.e., $\boldsymbol{G}\boldsymbol{v}_1 = \boldsymbol{v}_2$, we have

$$\|\boldsymbol{G}\|_{2,i} \geq \|\boldsymbol{v}_2\|/\|\boldsymbol{v}_1\| \triangleq \sigma_1. \tag{27}$$

This shows that $\sigma_1$ is a lower bound of $\|\boldsymbol{G}\|_{2,i}$. We then show that this lower bound can be achieved by the design given in (25). In this case,

$$\boldsymbol{G} = \begin{bmatrix} \boldsymbol{g}_2 \\ \boldsymbol{g}_3 \end{bmatrix} = \frac{1}{\|\boldsymbol{\psi}_{a0}\|^2} \begin{bmatrix} 2\zeta_2\omega_2\boldsymbol{\psi}_{a0}^T\boldsymbol{J} \\ \omega_2^2\boldsymbol{\psi}_{a0}^T\boldsymbol{J} \end{bmatrix} = \frac{\boldsymbol{v}_2\boldsymbol{v}_1^T}{\|\boldsymbol{v}_1\|^2}, \tag{28}$$

and it is clear that the design $\boldsymbol{G}$ satisfies the equality constraint $\boldsymbol{G}\boldsymbol{v}_1 = \boldsymbol{v}_2$ because

$$\boldsymbol{G}\boldsymbol{v}_1 = \frac{\boldsymbol{v}_2\boldsymbol{v}_1^T}{\|\boldsymbol{v}_1\|^2}\boldsymbol{v}_1 = \boldsymbol{v}_2\frac{\boldsymbol{v}_1^T\boldsymbol{v}_1}{\|\boldsymbol{v}_1\|^2} = \boldsymbol{v}_2. \tag{29}$$

Subsequently, with the expression (28), we have

$$\boldsymbol{G}^T\boldsymbol{G} = \frac{\boldsymbol{v}_1\boldsymbol{v}_2^T}{\|\boldsymbol{v}_1\|^2}\frac{\boldsymbol{v}_2\boldsymbol{v}_1^T}{\|\boldsymbol{v}_1\|^2} = \frac{\|\boldsymbol{v}_2\|^2}{\|\boldsymbol{v}_1\|^2}\frac{\boldsymbol{v}_1\boldsymbol{v}_1^T}{\|\boldsymbol{v}_1\|^2} = \sigma_1^2\frac{\boldsymbol{v}_1\boldsymbol{v}_1^T}{\|\boldsymbol{v}_1\|^2} \tag{30}$$

Therefore, $\boldsymbol{G}^T\boldsymbol{G}$ is a matrix with rank 1, which means that the eigenvalues of $\boldsymbol{G}^T\boldsymbol{G}$ are $(\sigma_1^2, 0)$, and the largest singular value of $\boldsymbol{G}$ is $\sigma_1$. Thus, the lower bound of $\|\boldsymbol{G}\|_{2,i}$ is achieved by this design.

## IV. ANALYSIS ON RELATIONSHIP BETWEEN OBSERVER GAINS AND EQUILIBRIA

In this section, we will analyze equilibria distribution and stability of the nonlinear estimation error dynamics. So far, the preceding research on linearization, estimation error dynamics, and parameter tuning strategy holds true for a neighborhood of the desired equilibrium $\boldsymbol{x}_0^* = \boldsymbol{0}$ defined in (12). Most of the previous studies assumed by default that $\boldsymbol{x}_0^*$ is the only equilibrium [20]–[22]. However, the error dynamics (11) may have other equilibria due to the nature of nonlinear systems. In particular, the choice of parameters $\zeta_1$ and $\omega_1$ affects the equilibria properties. We thus want to ensure that except the desired $\boldsymbol{x}_0^*$, all the other equilibria are unstable so that the estimation error will always converge to 0, i.e., to obtain an unbiased observer.

The objective of this section is to rule out all stable equilibria caused by gain parameter designs but not by model uncertainties. Thus, accurate model parameters are used in the following.

For the simplicity of illustration, we consider the linear error feedback law in (11), that is, replacing the nonlinear function fal($\boldsymbol{e}$) by linear function $\boldsymbol{e}$. Now denote the right hand side of (11) as $f$ and the equilibria can be obtained by solving the algebraic equation $f = 0$, which indicates that all the error dynamics vanish. With the design of the gain matrix as $\boldsymbol{G}_1 = [g_1, g_2]^T[1, -\beta]$, $\beta = -\psi_{aq0}/\psi_{ad0}$, we have

$$-\omega\boldsymbol{J}\tilde{\boldsymbol{\psi}} - \boldsymbol{G}_1\boldsymbol{L}\tilde{\boldsymbol{i}} = 0, \tag{31a}$$

$$\boldsymbol{\psi}_{a0}^T\boldsymbol{J}\boldsymbol{L}\tilde{\boldsymbol{i}} = 0. \tag{31b}$$

From (5) and (10e), we can express $\boldsymbol{i}$ and $\hat{\boldsymbol{i}}$ in terms of $\boldsymbol{\psi}$, $\hat{\boldsymbol{\psi}}$, and $\tilde{\theta}$ as

$$\boldsymbol{i} = e^{\tilde{\theta}\boldsymbol{J}}\boldsymbol{L}^{-1}e^{-\tilde{\theta}\boldsymbol{J}}\boldsymbol{\psi} - e^{\tilde{\theta}\boldsymbol{J}}\boldsymbol{L}^{-1}\boldsymbol{\psi}_f, \tag{32a}$$

$$\hat{\boldsymbol{i}} = \boldsymbol{L}^{-1}(\hat{\boldsymbol{\psi}} - \boldsymbol{\psi}_f). \tag{32b}$$

Subtracting (32b) from (32a), we get the flux estimation error as

$$\tilde{\boldsymbol{\psi}} = \boldsymbol{L}\tilde{\boldsymbol{i}} + (e^{\tilde{\theta}\boldsymbol{J}}\boldsymbol{L}e^{-\tilde{\theta}\boldsymbol{J}} - \boldsymbol{L})\boldsymbol{i} + (e^{\tilde{\theta}\boldsymbol{J}} - \boldsymbol{I})\boldsymbol{\psi}_f. \tag{33}$$

Substituting the expression of $\tilde{\boldsymbol{\psi}}$ in (33) into (31a) results in 3 equations and 3 unknowns $\tilde{i}_d$, $\tilde{i}_q$, and $\tilde{\theta}$. We then eliminate $\tilde{i}_d$

and $\tilde{i}_q$ to get the following equation on $\tilde{\theta}$ only[2]:

$$p_1 \cos 2\tilde{\theta}_0 + p_2 \sin 2\tilde{\theta}_0 + p_3 \cos \tilde{\theta}_0 + p_4 \sin \tilde{\theta}_0 + p_5 = 0, \tag{34}$$

where

$$p_1 = \Delta L \left[ (\beta i_d - i_q)\hat{\omega} + (\beta^2 + 1)(g_1 i_d - g_2 i_q) \right],$$
$$p_2 = \Delta L \left[ (\beta i_q + i_d)\hat{\omega} + (\beta^2 + 1)(g_2 i_d + g_1 i_q) \right],$$
$$p_3 = \psi_f \left[ \beta \hat{\omega} + (\beta^2 + 1)g_1 \right],$$
$$p_4 = \psi_f \left[ \hat{\omega} + (\beta^2 + 1)g_2 \right],$$
$$p_5 = -p_1 - p_3, \quad \Delta L = (L_d - L_q)/2. \tag{35}$$

To solve (34), we let $t = \tan(\tilde{\theta}_0/2)$ and then have

$$\sin \tilde{\theta}_0 = \frac{2t}{1+t^2}, \ \cos \tilde{\theta}_0 = \frac{1-t^2}{1+t^2}. \tag{36}$$

Substituting (36) into (34), we obtain a 4th-order polynomial equation. This can be easily solved by numerical packages, which in turn yield all the equilibria of error dynamics (11).

Since $\tilde{\theta}_0 = 0$ is a root for the original (34), $t = 0$ is indeed a root for the 4th-order polynomial equation after substitution. Other than the root at 0, it is evident that there may exist either 1 or 3 real roots due to $\tilde{\theta}_0$ is real. The Hartman-Grobman Theorem tells us that under some mild conditions, the dynamical behavior for a nonlinear system around an equilibrium is similar to its linearized version [35]. Therefore, from the parameter tuning strategy in the preceding section, we know that $\tilde{\theta}_0 = 0$ is a stable equilibrium that guarantees the local convergence of estimation errors. For the remaining 1 or 3 nonzero equilibria, we want all of them to be unstable such that the estimation error will diverge from them to avoid static estimation errors.

To determine the stability of a given equilibrium at $x_0$, we need to derive the Jacobian matrix of the system dynamics around $x_0$

$$J = \left. \frac{\partial f(\omega_0)}{\partial x} \right|_{x_0}. \tag{37}$$

If the Jacobian matrix $J$ is unstable, *i.e.*, some of its eigenvalues have non-negative real parts, the original nonlinear error dynamics is unstable in the vicinity of $x_0$. In practice, the analytic derivation of the Jacobian matrix $J$ at a nonzero equilibrium is highly complicated, we thus resort to numerical methods to compute it.

From (35), the equilibria of a specified operating point are affected by the feedback gains $g_1$ and $g_2$, which are in turn set by the desired damping ratio $\zeta_1$ and natural frequency $\omega_1$ through (16). It is then clear that these two flux related design parameters affect the equilibria distributions and stabilities. We thus want to find $\zeta_1$ and $\omega_1$ such that all the nonzero equilibria are unstable to obtain a feasible design, no matter there exists either 1 or 3 nonzero equilibria. If any of the resulting nonzero equilibria is stable, this corresponds to an infeasible design.

TABLE I
MODEL PARAMETERS FOR A PMSM

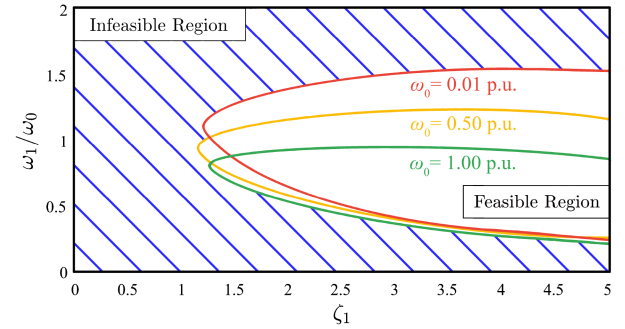| | |
|---|---|
| Stator resistance $R_s$ | 0.78 Ω |
| Direct-axis inductance $L_d$ | 2.46 mH |
| Quadrature-axis inductance $L_d$ | 2.68 mH |
| Permanent-magnet flux $\psi_f$ | 0.056 V·s |
| Pole pairs $p$ | 5 |
| Rated speed $\omega_r$ | 2400 rpm |
| Rated torque $T_r$ | 2.4 N·m |
| Rated dc-link voltage | 311 V |
| Rated RMS current | 4.8 A |
| Rated Power | 750 W |



Fig. 1. Equilibrium analysis results. The region bounded by the red edge represents the feasible design for $\omega_0 = 0.01$ p.u., the yellow the feasible region for $\omega_0 = 0.50$ p.u., and the green the feasible region for $\omega_0 = 1.00$ p.u. The blue region represents the infeasible design.

To illustrate this idea, we now consider a PMSM with the motor parameters given in Table I. Note that this is the same PMSM that will be used for experimental investigations in Section VI. We study three typical operations, namely, low speed $\omega_0 = 0.01$ p.u., medium speed $\omega_0 = 0.5$ p.u., and high speed $\omega_0 = 1$ p.u. In each case, for damping ratio $\zeta_1 \in [0, 5]$ and natural frequency $\omega_1/\omega_0 \in [0, 2]$, we compute the equilibria distribution and stability. The results are given in Fig. 1. The feasible region represents that all of the nonzero equilibria are unstable, whether there are 1 or 3 of them. In the infeasible region, there exists at least 1 stable nonzero equilibrium, and we want to keep away from these parameter designs to avoid static estimation errors. For any given PMSM drive with known motor parameters and given operating condition, it is always possible to compute the feasible and infeasible regions.

We therefore want to design $\zeta_1$ and $\omega_1$ to stay within the feasible region, which guarantees that the desired equilibrium $x_0^*$ with $\tilde{\theta}_0 = 0$ is the only stable equilibrium. Note that the aforementioned analysis is valid for linear magnetic machines. In practice, the inductance of the motor can vary in the circumstance of magnetic saturation and cross-saturation. Thus, we established a robust parameter tuning strategy for the flux estimation under inductance uncertainties. In detail, for a given operating point shown in Fig. 1, the gain parameters $\zeta_1$ and $\omega_1$ are chosen in the middle of the feasible region, i.e., to be far away from the boundary. This way, it can provide a large feasibility margin to counteract the inductance uncertainties due

---

[2]The structure of the steady-state error (34) is similar to [22]; however, the co-efficients (35) are in a more complicated form due to the different speed/position estimation law.

to magnetic saturation. Based on our numerical simulations and experimental experiences, parameters $\zeta_1$ and $\omega_1$ are suggested as

$$\zeta_1 = 1.5 + \omega_0/\omega_r, \quad \omega_1 = 1.5\omega_0/\zeta_1, \tag{38}$$

where $\omega_r$ is the rated speed.

## V. GLOBAL CONVERGENCE ANALYSIS

So far the preceding discussions are based on the assumption that the position observer is running at a constant velocity. In engineering practice, it is usually desired that the motor can track a time-varying speed profile with global convergence. In this section, we will show that the techniques developed earlier can be effectively extended to track speed trajectories as well. Meanwhile, we will prove that the proposed flux-based position observer is globally convergent.

For the constant velocity case, we use the linearization method to obtain a time invariant system (11), whose poles can be chosen to ensure that the estimation error converges to 0. Now for the time varying velocity case, i.e., $\dot{\omega} \neq 0$, the system equilibria and error dynamics in (11) are also time varying. Therefore the analysis for the position observer at constant velocity cannot be directly applied to the time varying case. Instead, we will apply the results of slowly varying system in nonlinear control theory [34] to show that the proposed position observer can be readily extended to the velocity tracking with stability guarantee.

At constant velocity, the estimation error dynamics in (11) can be rewritten as

$$\dot{\boldsymbol{x}} = f(\boldsymbol{x}, \omega_0). \tag{39}$$

Now for a time varying speed trajectory $\omega(t)$, the error dynamics (39) becomes

$$\dot{\boldsymbol{x}} = f(\boldsymbol{x}, \omega(t)). \tag{40}$$

The equilibrium of the system (40) is a function of $\omega$, thus we denote it as $\boldsymbol{x}_0 = h(\omega(t))$. Choosing appropriate gain parameters as in Sections III and IV, we can ensure that $\boldsymbol{x}_0 = \boldsymbol{0}$ is always the only stable equilibrium for any speed $\omega$ in the operating range $\Omega = \{\omega : 0 < \omega \leq \omega_{\max}\}$.

It is well known that the flux and current dynamics can achieve their steady states within several microseconds, whereas the rotor speed $\omega$ responds at a much slower time scale due to the large time constant of the mechanical system. Therefore, the rotor speed can be treated as a slowly varying variable in comparison with the fast electromagnetic dynamics. We can then use the mature results of slowly varying system to show that the proposed position observer is globally convergent.

Theorem 9.3 in [34]. *Consider a general system*

$$\dot{x} = f(x, u(t)). \tag{41}$$

*The change of variables $z = x - h(u)$ changes (41) into the form*

$$\dot{z} = g(z, u) - \frac{\partial h}{\partial u}\dot{u} \tag{42}$$

*Suppose $\|\partial h/\partial u\| \leq L, \forall u \in \Gamma$, $\|\dot{u}(t)\| \leq \varepsilon$ for all $t \geq 0$, and there is a Lyapunov function $V(z, u)$ that satisfies*

$$c_1\|z\|^2 \leq V(z, \alpha) \leq c_2\|z\|^2, \tag{43a}$$

$$\frac{\partial V}{\partial z}g(z, \alpha) \leq -c_3\|z\|^2, \tag{43b}$$

$$\left\|\frac{\partial V}{\partial z}\right\| \leq c_4\|z\|, \tag{43c}$$

$$\left\|\frac{\partial V}{\partial \alpha}\right\| \leq c_5\|z\|^2, \tag{43d}$$

*for all $z \in D = \{z \mid \|z\| < r\}$ and $\alpha \in \Gamma$, where $c_i$ values are positive constants independent of $\alpha$. If*

$$\varepsilon < \frac{c_1 c_3}{c_2 c_5}\frac{r}{r + c_4 L/c_5}, \tag{44}$$

*then for all $\|z(0)\| < r\sqrt{c_1/c_2}$, the solutions of the system are uniformly bounded for all $t \geq 0$ and uniformly ultimately bounded by*

$$b = \frac{c_2 c_4 L\varepsilon}{\theta(c_1 c_3 - \varepsilon c_2 c_5)}, \tag{45}$$

*where $\theta \in (0, 1)$ is an arbitrary constant. If in addition, $\dot{u}(t) \to 0$ as $t \to \infty$, then $z(t) \to 0$ as $t \to \infty$. Finally, if $h(u) = 0$ for all $u \in \Gamma$ and $\varepsilon < c_3/c_5$, then $z = 0$ is an expoentially stable equilibrium point of (42). Equivalently, $x = 0$ is an exponentially stable equilibrium point of (41).*

Hereafter we prove that the proposed position observer is globally convergent for time-varying speed $\omega$ by using this Theorem. Note that the origin is always the only stable equilibrium by our tuning strategy, i.e., $h(\omega(t)) = 0$, so we don't need to do the change of variables as in the Theorem. Thus, the estimation error dynamics (40) can be written as

$$\dot{\boldsymbol{z}} = g(\boldsymbol{z}, \omega), \tag{46}$$

where the second term in (42) vanishes due to $\partial h/\partial \omega = 0$.

The general idea of the proof is to construct a Lyapunov function and show that all the conditions (43) in the above Theorem are satisfied. The Lyapunov function needs to be positive definite as in (43a) and its derivative along the dynamical trajectory of the system is negative definite as in (43b). Inequalities (43c) and (43d) are required to handle the perturbations, which come from the fact that $\omega$ is a time varying function. The special requirement is that these inequalities hold uniformly for any $\omega_0 \in \Omega$.

Now we construct the Lyapunov function $V(z, \omega)$ as

$$V(\boldsymbol{z}, \omega) = \boldsymbol{z}^T P(\omega)\boldsymbol{z}, \tag{47}$$

where $P(\omega)$ is the solution of the following Lyapunov equation

$$PA(\omega) + A^T(\omega)P = -I, \tag{48}$$

and $A(\omega)$ is the system matrix given in (15). From our parameter tuning strategy, for a specific operating speed $\omega_0$, the elements of $A(\omega_0)$ and their first partial derivatives with respect to each $\omega_0$ are uniformly bounded, that is,

$$\|A(\omega_0)\|_2 \leq \rho, \quad \left\|\frac{\partial A(\omega_0)}{\partial \omega_0}\right\|_2 = 1, \quad \forall \omega_0 \in \Omega. \tag{49}$$

Moreover, the tuning strategy also guarantees that $A(\omega_0)$ is Hurwitz uniformly in $\omega_0$ and satisfies

$$\text{Re}\left[\lambda\left(A(\omega_0)\right)\right] \leq \sigma < 0, \quad \forall \omega_0 \in \Omega. \tag{50}$$

Thus, the Lyapunov (48) always has a unique positive definite solution $P(\omega_0)$ for each $A(\omega_0)$.

We can show that if $\|\boldsymbol{z}\|_2 < (1 - c_3)/(2c_2 k_1)$, the Lyapunov function $V(\boldsymbol{z}, \omega_0)$ satisfies all of the inequalities in (43) for all $\omega_0$, with

$$c_1 = \frac{1}{2\rho}, \quad c_2 = \frac{k^2}{2\gamma}, \quad c_3 > 0, \quad c_4 = \frac{k^2}{\gamma}, \quad c_5 = \frac{k^4}{2\gamma^2}. \tag{51}$$

Detailed procedure to show that the inequality conditions (43) are satisfied is provided in Appendix A.

Finally, the changing rate of the speed $|\dot{\omega}|$ cannot be too large. Indeed, it is restricted by the following constraint:

$$|\dot{\omega}| \leq \varepsilon < \frac{c_3}{c_5} = 2c_3 \frac{\gamma^2}{k^4}. \tag{52}$$

To estimate a time varying speed with a moderate speed derivative, we require a larger $\gamma$. This can be realized by placing the eigenvalues of $A(\omega)$ far away from the imaginary axis in the complex plane.

Combining all these results, we conclude that for all the initial states with $\|\boldsymbol{x}(0)\| < r\sqrt{c_1/c_2}$, the equilibrium $\boldsymbol{x} = 0$ is exponentially stable for the slowly varying system (40). Therefore, our observer can track a time-varying speed trajectory in the large signal sense, which means the system is globally convergent even during the transient.

*Remark 1:* The initial condition $\|\boldsymbol{x}(0)\| < r\sqrt{c_1/c_2}$ can be satisfied by choosing a good initial guess of the position. This can be achieved by using HFI method for IPM [13], or some other start-up strategies for SPM [19], [36].

*Remark 2:* Due to the similar mechanism of the flux-based observers, the global stability proof presented in this section can be easily extended to those in [21], which thus provides a needed but overlooked feature for the existing observers.

*Remark 3:* Magnetic saturation and cross-saturation effects are not considered in this section. Stability analysis including the saturation effects is reported in [30].

## VI. Experimental Results

We now perform experiments to demonstrate the effectiveness of the proposed position observer.

### A. Experimental Setup

We use the same 750 W PMSM as discussed in Section IV, whose model parameters are given in Table I. The controller is implemented on a DSP board with the micro control unit (MCU) STM32F407. The phase currents and dc-link voltage are measured by sampling circuits on the DSP board with 8 kHz sampling frequency. For reference purposes, the rotor position and speed are measured by a 17-bit absolute encoder. The space vector PWM (SVPWM) technique is applied to drive the PMSM, and the dead time effect and inverter nonlinearities are compensated by the methods given in [37]. The loading system is a high dynamical servo system that can imitate different working conditions.

For sensorless PMSM drives, a common cascaded controller is applied in our experiments. The inner loop controls the current, and the outer one controls the speed. Both loops use the PI control algorithms. The controller for current is implemented in the estimator frame, and the rotor position and speed are estimated by the position observer (10). In our investigation, the bandwidths of the current controller and the speed controller are designed as 500 Hz and 5 Hz, whereas the observer bandwidth of each experiment is specified in Section VI-B.

### B. Results and Discussions

Firstly, we show the performance of the position observer when the motor is controlled to track a 10 Hz ($\omega = 0.05$ p.u.) ramp-up speed profile. Here, the observer bandwidth is set as 50 Hz, which is the same value used in the following experiments in Figs. 3–6. The loading system is enabled with a constant load torque $T_L = 0.1$ p.u. Fig. 2(a) shows that the observer generates position estimation that quickly converges to the real value. In Fig. 2(b), we observe that the initial estimation error $\tilde{\theta}(0)$ is about $30°$, and the estimation error decreases to 0 after 0.35 s. The mean value and standard deviation of the estimation error in steady state are $0.11°$ and $0.69°$, respectively. The speed tracking error in steady state Fig. 2(c) is within $\pm 5\%$ range.

Then, we show that the proposed position observer works well in both the low speed $\omega = 0.01$ p.u. and the rated speed $\omega = 1.00$ p.u. For the low speed case $\omega = 0.01$ p.u. with 1% rated load, Fig. 3(a) shows the estimation error at steady state, where the mean value and standard deviation are $1.45°$ and $0.10°$, respectively. The speed tracking performance in steady state is shown in Fig. 3(b), where the speed is fluctuating around the reference value within $\pm 15\%$ bound. Note that the mean value of the estimation error is nonzero, and the tracking error percentage is relatively large. This is caused by the adverse effects of dead time, inverter nonlinearities, and low signal to noise ratio (SNR), which is particularly apparent in the low speed range. This error can be further reduced by more sophisticated compensation techniques.

For the rated speed operation $\omega = 1.00$ p.u. with rated load, shown in Fig. 4(a), we can see that the mean value and the standard deviation of the position estimation error are $0.07°$ and $0.08°$, respectively, which are much better than those in the low speed operation. This demonstrates that the dead time, inverter nonlinearities and SNR have less significance in high speed range. Furthermore, as shown in Fig. 4(b), the speed control shows a better steady-state performance with tracking error fluctuating within $\pm 1\%$ bound.

Now, we investigate the promptness of the sensorless system. The motor was controlled to track a step speed reference profile without load. The speed reference steps up from 0 p.u. to 1.0 p.u. and later steps down from 1.0 p.u. to 0.5 p.u. Fig. 5(a) shows that the speed estimation from the proposed observer can track the real speed closely and smoothly, and the corresponding position estimation error is illustrated in Fig. 5(b).
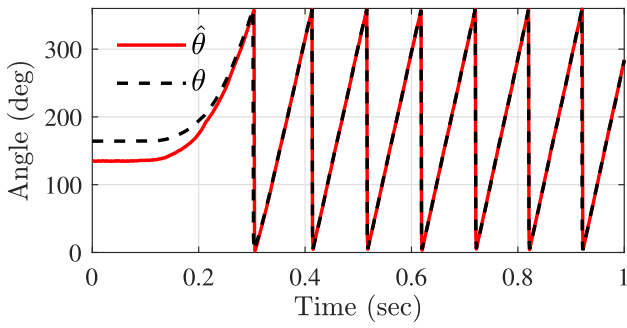
(a)
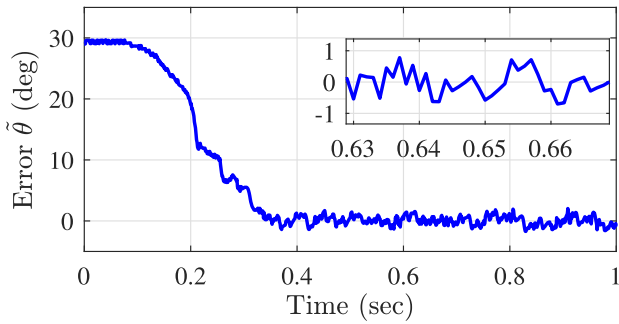


(b)
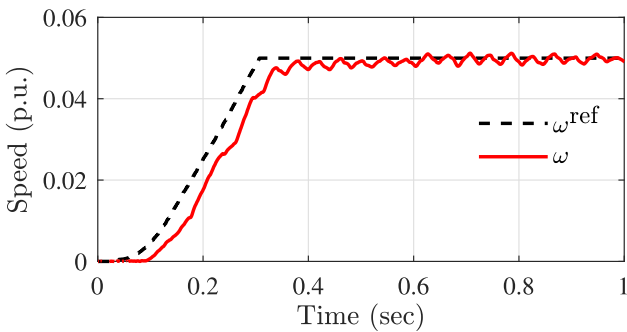


(c)

Fig. 2. Performance of the position observer in a loaded ramp-up operation. (a) The black line represents the real rotor position measured by encoder, and the red line the estimated position from the observer. (b) The position estimation error $\tilde{\theta}$. (c) The black line is the reference speed trajectory, and the red line the achieved speed.

Subsequently, we evaluate the dynamic response of the observer to the step load torque command. At first, the motor ran at a steady-state $\omega_0 = 1.0$ p.u. Then, the loading system was enabled with a load torque command $T_L = 0.25$ p.u. at $t = 0.5$s. As shown in Fig. 6, the speed drops instantaneously and then recovers to the nominal reference value. At $t = 2.25$s, we applied an exciting torque with $T_L = -0.25$ p.u. It can be seen that the speed hikes up at once and then recovers to its maintained value. In both cases, the proposed observer can effectively estimate the real speed even subject to sudden load changes.

In the following, we illustrate that the proposed nonlinear position observer (10) has better noise suppression capability
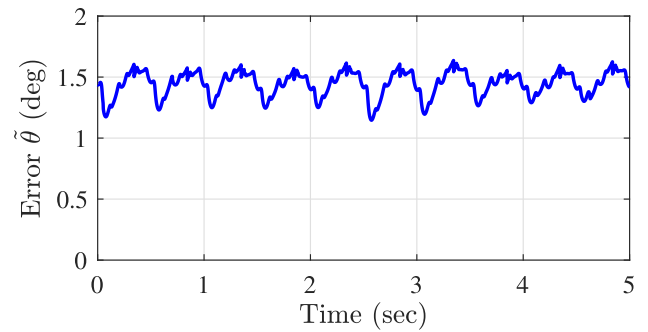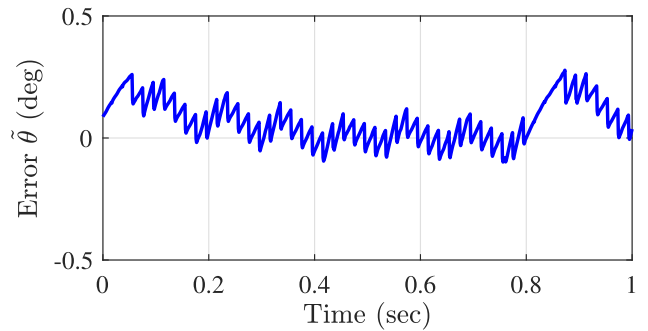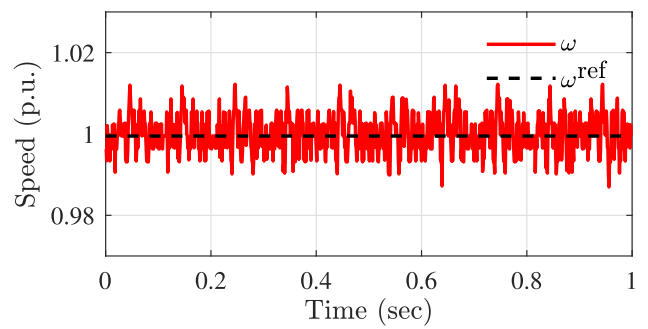


(a)
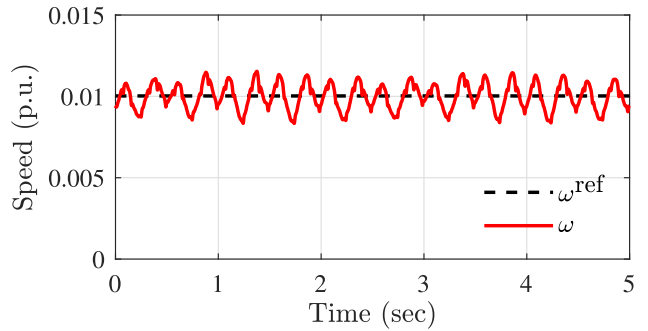


(b)

Fig. 3. Performance of the position observer at the low speed operating point $\omega = 0.01$ p.u. (a) The steady-state position estimation error. (b) The black line is the speed reference, and the red line the achieved speed.



(a)



(b)

Fig. 4. Performance of the position observer at the rated speed operating point $\omega = 1.00$ p.u. (a) The steady-state position estimation error. (b) The black line is the speed reference, and the red line the achieved speed.
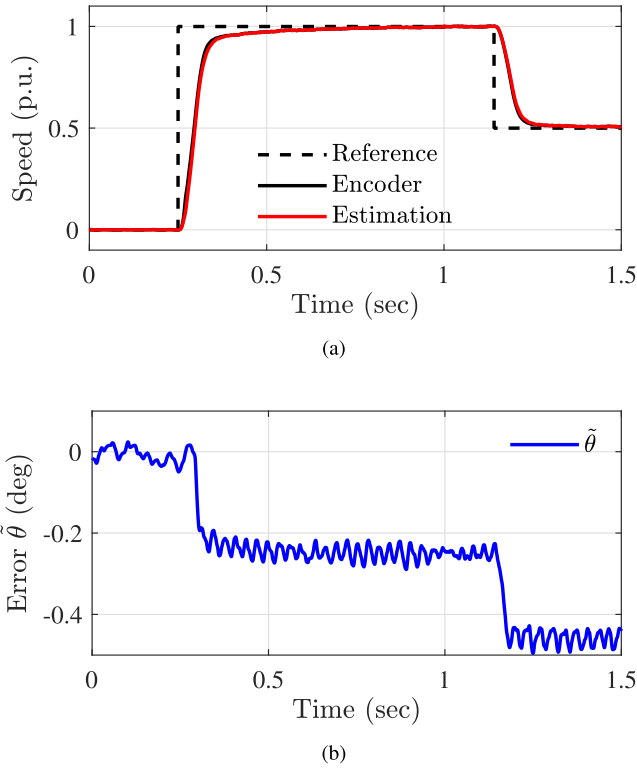
Fig. 5. Dynamic response to step reference in speed without load. (a) Speed tracking and estimation performance. (b) Position estimation error.
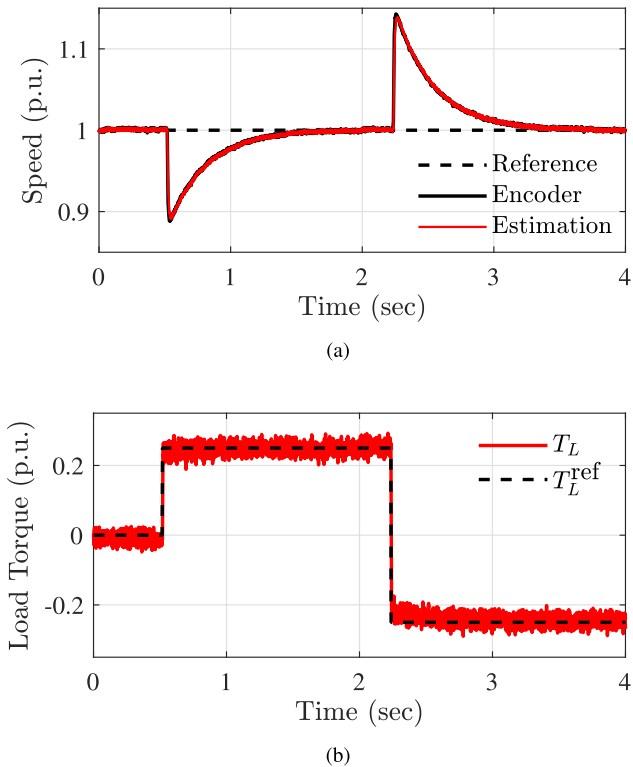


Fig. 6. Dynamic response to step reference in load torque command. (a) Speed tracking and estimation performance. (b) Load torque measured by torsion-bar.
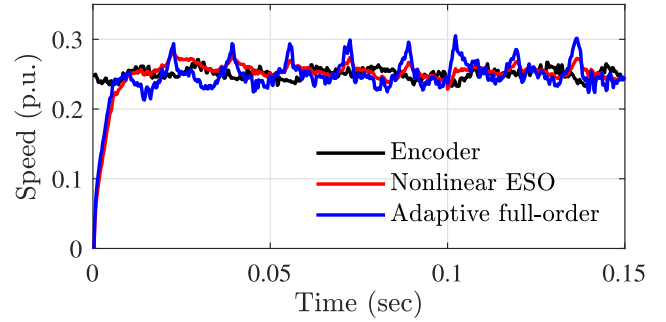


Fig. 7. Noise suppression comparison between the proposed nonlinear observer (10) and adaptive full-order observer [21] when their dynamic responses are approximately the same fast.
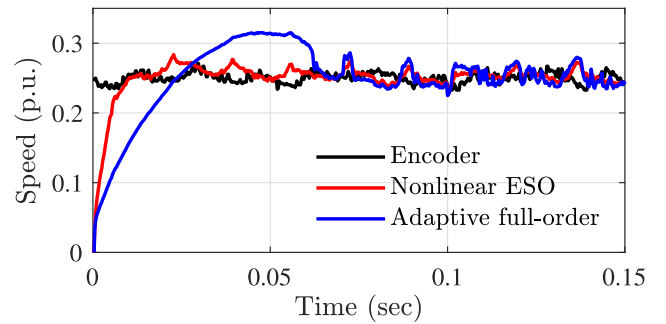


Fig. 8. Dynamic response comparison between the proposed nonlinear observer (10) and adaptive full-order observer in [21] when their steady-state fluctuations are more or less at the same level.

and faster dynamic response in Figs. 7 and 8 when compared with the adaptive full-order observer in [21]. The speed/position estimator designed in [21] is given by

$$\hat{\omega} = k_p \tilde{\tilde{i}}_d + k_i \int \tilde{\tilde{i}}_d dt, \quad \dot{\hat{\theta}} = \hat{\omega}, \tag{53}$$

where $k_p = 2\omega_2/\psi_{ad0}$ and $k_i = \omega_2^2/\psi_{ad0}$.

To demonstrate these advantages, we ran the motor in sensing mode, and the real rotor position reading from the encoder is used in Park transformation for control, which is different from the experiments in the sensorless mode shown in Figs. 2–6. In more detail, the position observer worked in open loop mode, i.e., its output of the estimated angle $\hat{\theta}$ was not used in the closed loop control, but is only used to transform the variables in the stator coordinate into the estimated rotor coordinate for observing purpose. In this case, the inputs to the position observer are the voltage $u$ and current $i$ in the estimated frame. Specifically, in Figs. 7 and 8, we first controlled the motor running at a steady-state $\omega_0 = 0.25$ p.u., and then started both observers from zero initial conditions. This way, we can evaluate their estimation performance subject to the step input.

When discussing the noise suppression in Fig. 7, we consider the intrinsic noises in the system, e.g., those noises from the current measurements. However, different observers have different noise suppression capabilities and thus can result in different fluctuation levels at steady-state. For a fair comparison, we set
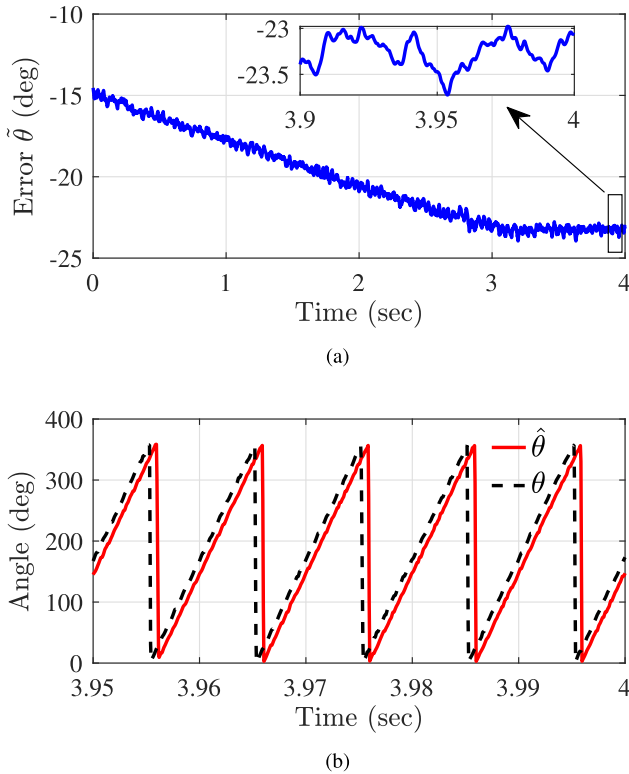
Fig. 9. Nonzero equilibrium (static position error) caused by infeasible design. (a) Settling procedure of a nonzero position error $\tilde{\theta}_0$. (b) Estimated position with infeasible design in steady state.
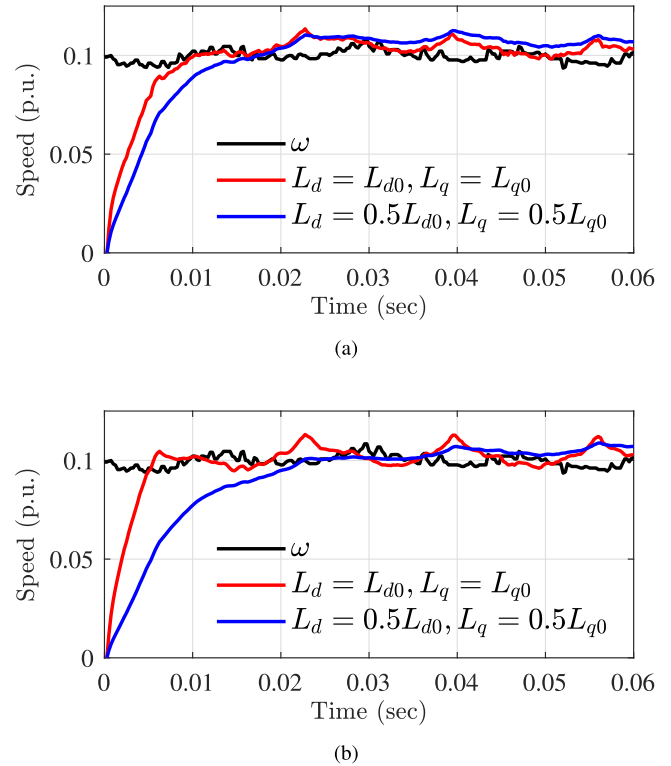


Fig. 10. Estimation performance comparison under model parameter uncertainties. (a) Proposed observer with optimal design (25). (b) Adaptive full-order observer [21].

the bandwidth of both observers as 250 Hz, which is large enough to obtain fast estimation dynamics. From Fig. 7, we observe that the dynamic responses of both observers are more or less the same fast, and our observer yields the speed estimation with smaller fluctuation. It thus indicates that the proposed nonlinear position observer can suppress the noise more effectively.

When discussing the fast dynamics in Fig. 8, we kept the bandwidth of the proposed nonlinear observer at 250 Hz as the same in Fig. 7, and reduced the bandwidth of the adaptive full-order observer to 150 Hz to obtain a small fluctuation. This way, the achieved steady-state fluctuations of both observers are more or less at the same level, and thus they have similar noise suppression capabilities. From Fig. 8, it can be seen that the proposed nonlinear position observer has a faster dynamic response with a smaller overshoot.

However, we would like to point out that the adaptive full-order observer has benefits on implementation convenience and computational efficiency.

Fig. 9 shows that inappropriate parameter design in the infeasible region will lead to nonzero steady-state estimation error as analyzed in Section IV. Specifically, we controlled the motor to ramp up to $\omega_0 = 0.5$ p.u. in sensorless mode, where the observer parameters $\zeta_1 = 0.5$ and $\omega_1 = 0.5\omega_0$ were intentionally chosen inside the infeasible design region in Fig. 1. The settling procedure to a nonzero equilibrium after a speed transient is shown in Fig. 9, whose initial position estimation error is $-14.53°$. The experimental results in Fig. 9 indicates a nonzero stable

equilibrium with static position error $\tilde{\theta}_0 \approx 23.18°$, which agrees well with the theoretical solution $20.91°$ calculated from (34) and (35).

As shown in Section III-B, the position/speed estimation law of the proposed observer is robust against the inductance parameter uncertainties. To better illustrate this optimal design (25), we performed a controlled experiment in Fig. 10(a), where the experimental setup is similar to that in Fig. 7. In more detail, the motor was controlled at $\omega_0 = 0.1$ p.u. in sensing mode, and the observer worked in open loop with its bandwidth set at 50 Hz. Then, the performance of the position observer was evaluated subject to such a step input. The proposed observer (10) was firstly implemented with accurate inductance parameter value, then with half of the nominal value respectively. The estimation performance of the proposed observer is given in Fig. 10(a). Subsequently, the adaptive full-order observer [21] was implemented under the same experimental setting, and its estimation performance is given in Fig. 10(b). We observe that performance of the proposed method is deteriorated but still acceptable under inductance variations, whereas the adaptive full-order observer results in slower dynamic response.

Finally, we compare the performance between the proposed observer with adaptation gains and the observer with fixed gains [17] under different operating points. Both observers were initialized with zero conditions. The proposed adaptive gains are given in (16) and (25), and adapt to different operating conditions automatically. For a fair comparison, the fixed gains in [17] were
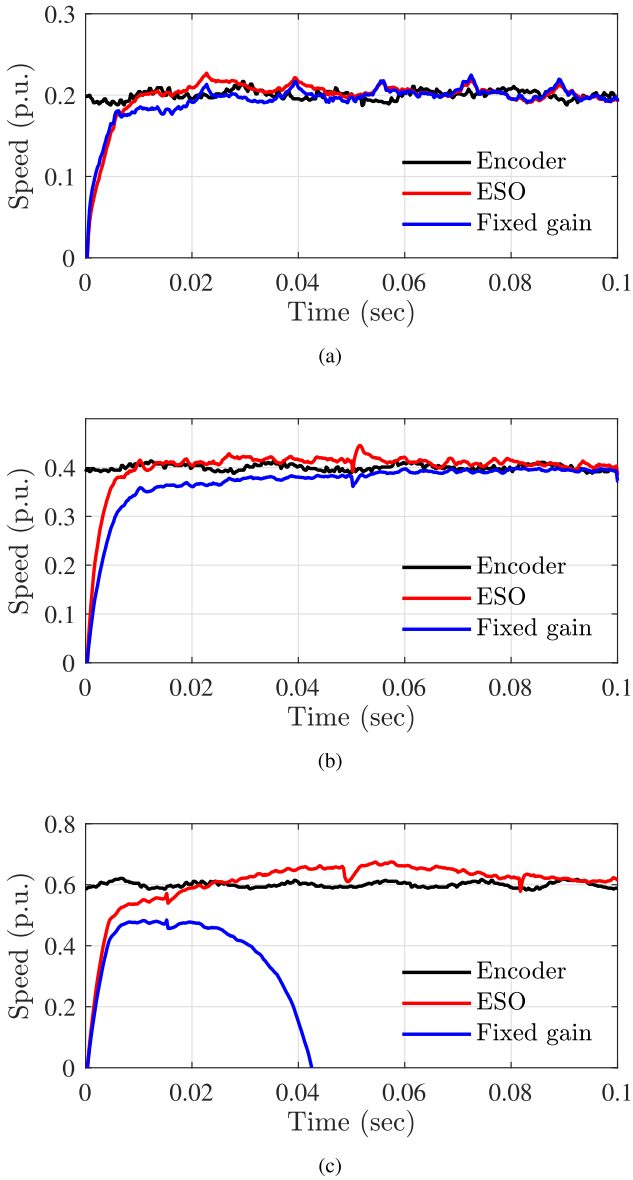
Fig. 11.   Estimation performance comparison between the proposed observer with adaptive gains (16), (25) and the fixed gains methods [17] under different operating points. (a) $\omega_0 = 0.2$ p.u. (b) $\omega_0 = 0.4$ p.u. (c) $\omega_0 = 0.6$ p.u.

carefully tuned to achieve a similar performance as the adaptive design at the operating condition $\omega_0 = 0.2$ p.u., as shown in Fig. 11(a), and remained the same for all three experiments. Then, the operating condition was set to $\omega_0 = 0.4$ p.u. From Fig. 11(b), both estimations can converge to the real speed. However, the fixed-gain design responds slower and needs a longer time to settle. When it comes to the operating condition $\omega_0 = 0.6$ p.u. in Fig. 11(c), the adaptive observer can still track the real speed with somewhat degraded performance, but the fixed gain design cannot converge at all.

## VII.  CONCLUSION

In this paper, we applied extended state observer to the position estimation of sensorless PMSM drives. Parameter tuning

strategy is established to obtain fast convergence of the error and robustness against model uncertainties and disturbances. Further, the equilibria distribution of the error dynamics is analyzed in detail, and our parameter design guarantees that the origin is invariably the desired stable equilibrium at any operating condition. Moreover, by treating the rotor speed as a slowly varying variable, we can readily extend the ESO estimator to the operation of velocity tracking. We proved the global stability of the proposed position observer, which is also applicable to those flux-based observers in literature. The overall performance of the proposed position observer was investigated on a 750 W PMSM drive. The experimental results showcased good estimation performance both in steady state and in transient phase, and the nonlinear observer was found to have faster convergence as well as better noise suppression.

## APPENDIX A
### PROOF OF THE INEQUALITIES (43)

Note that the Jacobian matrix of $g(\boldsymbol{z}, \omega)$ at the equilibrium $\boldsymbol{x}_0$ is actually the system matrix $A(\omega_0)$ of the linearized estimation error dynamics (15). If the slowly varying variable $\omega$ is fixed at $\omega_0$, then the dynamics of (46) can be rewritten as an equivalent form in (54),

$$\dot{\boldsymbol{z}} = A\boldsymbol{z} + [g(\boldsymbol{z}, \omega_0) - A\boldsymbol{z}] = A\boldsymbol{z} + \Delta g(\boldsymbol{z}, \omega_0), \quad (54)$$

with the assumption that $\|\Delta g(\boldsymbol{z}, \omega_0)\|_2 \le k_1 \|\boldsymbol{z}\|_2^2$ for all $\boldsymbol{z} \in D = \{\boldsymbol{z} \mid \|\boldsymbol{z}\| \le r\}$. We then show the inequalities (43) are all satisfied.

1) Inequality (43a) Since $A(\omega_0)$ is Hurwitz, in addition, $\|A(\omega_0)\|_2 \le \rho$, and $\text{Re}[\lambda(A(\omega_0))] \le \sigma < 0$ uniformly in $\omega_0$, by applying Gronwall-Bellman inequalities, we can find positive constants $k$ and $\gamma$ independent of $\omega_0$ such that

$$\|e^{tA(\omega_0)}\| \le ke^{-\gamma t}, \quad \forall t \ge 0, \forall \omega_0 \in \Gamma. \quad (55)$$

Moreover, the solution $P(\omega_0)$ of the Lyapunov equation can be represented by

$$P(\omega_0) = \int_0^\infty \left[ e^{tA(\omega_0)} \right]^T \left[ e^{tA(\omega_0)} \right] dt, \quad (56)$$

then,

$$V(\boldsymbol{z}, \omega_0) = \boldsymbol{z}^T P(\omega_0) \boldsymbol{z} \le \int_0^\infty k^2 e^{-2\gamma t} \|\boldsymbol{z}\|_2^2 \, dt,$$

$$= \frac{k^2}{2\gamma} \|\boldsymbol{z}\|_2^2 = c_2 \|\boldsymbol{z}\|_2^2. \quad (57)$$

Since $P(\omega_0)$ is positive definite, from the results in [34], we have

$$\boldsymbol{z}^T P(\alpha) \boldsymbol{z} \ge \frac{1}{2\rho} \|\boldsymbol{z}\|_2^2 = c_1 \|\boldsymbol{z}\|_2^2. \quad (58)$$

2) Inequality (43b) Subsequently, taking derivative of the Lyapunov function candidate, it is obtained that

$$
\begin{aligned}
\dot{V}(\boldsymbol{z}, \omega_0) &= \dot{\boldsymbol{z}}^T P(\omega_0) \boldsymbol{z} + \boldsymbol{z}^T P(\omega_0) \dot{\boldsymbol{z}} \\
&= (A(\omega_0) \boldsymbol{z} + \Delta g(\boldsymbol{z}, \omega_0))^T P(\omega_0) \boldsymbol{z} \\
&\quad + \boldsymbol{z}^T P(\omega_0)(A(\omega_0) \boldsymbol{z} + \Delta g(\boldsymbol{z}, \omega_0)) \\
&= -\boldsymbol{z}^T \boldsymbol{z} + \Delta g(\boldsymbol{z}, \omega_0)^T P(\omega_0) \boldsymbol{z} \\
&\quad + \boldsymbol{z}^T P(\omega_0) \Delta g(\boldsymbol{z}, \omega_0) \\
&= -\boldsymbol{z}^T \boldsymbol{z} + 2\Delta g(\boldsymbol{z}, \omega_0)^T P(\omega_0) \boldsymbol{z} \\
&\leq -\|\boldsymbol{z}\|_2^2 + 2c_2 k_1 \|\boldsymbol{z}\|_2^3 \leq -c_3 \|\boldsymbol{z}\|_2^2, \quad (59)
\end{aligned}
$$

for $\|\boldsymbol{z}\|_2 < (1 - c_3)/(2c_2 k_1)$.

3) Inequality (43c) Further, from the results of (57), we have

$$
\begin{aligned}
\left\| \frac{V(\boldsymbol{z}, \omega_0)}{\partial \boldsymbol{z}} \right\|_2 &= \left\| \frac{\partial \boldsymbol{z}^T P(\omega_0) \boldsymbol{z}}{\partial \boldsymbol{z}} \right\|_2 = \|2P(\omega_0)\boldsymbol{z}\|_2 \\
&\leq 2c_2 \|\boldsymbol{z}\|_2 = c_4 \|\boldsymbol{z}\|_2. \quad (60)
\end{aligned}
$$

4) Inequality (43d) For the last inequality, we differentiate (48) partially with respect to $\omega_0$, and denote the derivative of $P(\omega_0)$ by $P'(\omega_0)$, and obtain

$$
\begin{aligned}
&P'(\omega_0) A(\omega_0) + A^T(\omega_0) P'(\omega_0) \\
&= -\left\{ P(\omega_0) A'(\omega_0) + [A'(\omega_0)]^T P(\omega_0) \right\} \triangleq -Q.
\end{aligned}
\tag{61}
$$

Thus, $P'(\omega_0)$ is given by

$$
P'(\omega_0) = \int_0^\infty \left[ e^{tA(\omega_0)} \right]^T Q \left[ e^{tA(\omega_0)} \right] \, dt. \tag{62}
$$

It follows that

$$
\|P'(\omega_0)\|_2 \leq \int_0^\infty k_2 e^{-2\gamma t} 2 \frac{k^2}{2\gamma} b \, dt = \frac{k^4}{2\gamma^2}, \tag{63}
$$

so the partial derivative of $V(\boldsymbol{z}, \omega_0)$ with respect to $\boldsymbol{z}$ satisfies

$$
\begin{aligned}
\left\| \frac{V(\boldsymbol{z}, \omega_0)}{\partial \omega_0} \right\|_2 &= \left\| \frac{\partial \boldsymbol{z}^T P(\omega_0) \boldsymbol{z}}{\partial \omega_0} \right\|_2 = \|\boldsymbol{z}^T P'(\omega_0) \boldsymbol{z}\|_2 \\
&\leq \frac{k^4}{2\gamma^2} \|\boldsymbol{z}\|_2^2 = c_5 \|\boldsymbol{z}\|_2^2. \quad (64)
\end{aligned}
$$

## REFERENCES

[1] M. P. Kazmierkowski, R. Krishnan, and F. Blaabjerg, *Control in Power Electron.*, New York, NY, USA: Elsevier, 2002.

[2] G. Wang, G. Zhang, and D. Xu, *Position Sensorless Control Techn. for Permanent Magnet Synchronous Machine Drives*, Berlin, Germany: Springer, 2020.

[3] K. H. Nam, *AC Motor Control and Electrical Vehicle Applications*, Boca Raton, FL, USA: CRC Press, 2018.

[4] R. Krishnan, *Permanent Magnet Synchronous and Brushless DC Motor Drives*, Boca Raton, FL, USA: CRC Press, 2017.

[5] H. Kim, J. Son, and J. Lee, "A high-speed sliding-mode observer for the sensorless speed control of a PMSM," *IEEE Trans. Ind. Electron.*, vol. 58, no. 9, pp. 4069–4077, Sep. 2011.

[6] Z. Qiao, T. Shi, Y. Wang, Y. Yan, C. Xia, and X. He, "New sliding-mode observer for position sensorless control of permanent-magnet synchronous motor," *IEEE Trans. Ind. Electron.*, vol. 60, no. 2, pp. 710–719, Feb. 2013.

[7] H. Lee and J. Lee, "Design of iterative sliding mode observer for sensorless PMSM control," *IEEE Trans. Control Syst. Technol.*, vol. 21, no. 4, pp. 1394–1399, Jul. 2013.

[8] J.-S. Kim and S.-K. Sul, "High performance PMSM drives without rotational position sensors using reduced order observer," in *Proc. IEEE 13th IAS Annu. Meeting Conf. Rec. Ind. Appl.*, 1995, vol. 1, pp. 75–82.

[9] T. Chan, W. Wang, P. Borsje, Y. Wong, and S. L. Ho, "Sensorless permanent-magnet synchronous motor drive using a reduced-order rotor flux observer," *IET Electric Power Appl.*, vol. 2, no. 2, pp. 88–98, 2008.

[10] S. Bolognani, R. Oboe, and M. Zigliotto, "Sensorless full-digital PMSM drive with EKF estimation of speed and rotor position," *IEEE Trans. Ind. Electron.*, vol. 46, no. 1, pp. 184–191, Feb. 1999.

[11] S. Bolognani, L. Tubiana, and M. Zigliotto, "Extended Kalman filter tuning in sensorless PMSM drives," *IEEE Trans. Ind. Appl.*, vol. 39, no. 6, pp. 1741–1747, Nov./Dec. 2003.

[12] M. Schroedl, "Sensorless control of AC machines at low speed and standstill based on the "INFORM" method," in *Proc. IEEE 31st IAS Annu. Meeting Conf. Rec. Ind. Appl.*, 1996, vol. 1, pp. 270–277.

[13] J.-H. Jang, J.-I. Ha, M. Ohto, K. Ide, and S.-K. Sul, "Analysis of permanent-magnet machine for sensorless control based on high-frequency signal injection," *IEEE Trans. Ind. Appl.*, vol. 40, no. 6, pp. 1595–1604, Nov./Dec. 2004.

[14] P. L. Jansen and R. D. Lorenz, "Transducerless position and velocity estimation in induction and salient AC machines," *IEEE Trans. Ind. Appl.*, vol. 31, no. 2, pp. 240–247, Mar./Apr. 1995.

[15] S. Koonlaboon and S. Sangwongwanich, "Sensorless control of interior permanent-magnet synchronous motors based on a fictitious permanent-magnet flux model," in *Proc. 40th IAS Annu. Meeting. Conf. Rec. Ind. Appl.*, 2005, vol. 1, pp. 311–318.

[16] A. A. Bobtsov, A. A. Pyrkin, R. Ortega, S. N. Vukosavic, A. M. Stankovic, and E. V. Panteley, "A robust globally convergent position observer for the permanent magnet synchronous motor," *Automatica*, vol. 61, pp. 47–54, 2015.

[17] E. Capecchi, P. Guglielmi, M. Pastorelli, and A. Vagati, "Position-sensorless control of the transverse-laminated synchronous reluctance motor," *IEEE Trans. Ind. Appl.*, vol. 37, no. 6, pp. 1768–1776, Nov./Dec. 2001.

[18] P. Guglielmi, M. Pastorelli, G. Pellegrino, and A. Vagati, "Position-sensorless control of permanent-magnet-assisted synchronous reluctance motor," *IEEE Trans. Ind. Appl.*, vol. 40, no. 2, pp. 615–622, Mar./Apr. 2004.

[19] L. Harnefors, M. Jansson, R. Ottersten, and K. Pietilainen, "Unified sensorless vector control of synchronous and induction motors," *IEEE Trans. Ind. Electron.*, vol. 50, no. 1, pp. 153–160, Feb. 2003.

[20] A. Piippo, M. Hinkkanen, and J. Luomi, "Analysis of an adaptive observer for sensorless control of interior permanent magnet synchronous motors," *IEEE Trans. Ind. Electron.*, vol. 55, no. 2, pp. 570–576, Feb. 2008.

[21] M. Hinkkanen, S. E. Saarakkala, H. A. A. Awan, E. Mölsä, and T. Tuovinen, "Observers for sensorless synchronous motor drives: Framework for design and analysis," *IEEE Trans. Ind. Appl.*, vol. 54, no. 6, pp. 6090–6100, Nov./Dec. 2018.

[22] T. Tuovinen, M. Hinkkanen, L. Harnefors, and J. Luomi, "Comparison of a reduced-order observer and a full-order observer for sensorless synchronous motor drives," *IEEE Trans. Ind. Appl.*, vol. 48, no. 6, pp. 1959–1967, Nov./Dec. 2012.

[23] A. Piippo, M. Hinkkanen, and J. Luomi, "Adaptation of motor parameters in sensorless PMSM drives," *IEEE Trans. Ind. Appl.*, vol. 45, no. 1, pp. 203–212, Jan./Feb. 2009.

[24] M. Hinkkanen, T. Tuovinen, L. Harnefors, and J. Luomi, "A combined position and stator-resistance observer for salient PMSM drives: Design and stability analysis," *IEEE Trans. Power Electron.*, vol. 27, no. 2, pp. 601–609, Feb. 2012.

[25] T. Tuovinen, H. A. Ali Awan, J. Kukkola, S. E. Saarakkala, and M. Hinkkanen, "Permanent-magnet flux adaptation for sensorless synchronous motor drives," in *Proc. IEEE 9th Int. Symp. Sensorless Control Elect. Drives*, 2018, pp. 138–143.

[26] G. Zhang, L. Yang, J. Zhang, and C. Han, "Longitudinal attitude controller design for aircraft landing with disturbance using ADRC/LQR," in *Proc. IEEE Int. Conf. Automat. Sci. Eng.*, 2013, pp. 330–335.

[27] S. E. Talole, J. P. Kolhe, and S. B. Phadke, "Extended-state-observer-based control of flexible-joint system with experimental validation," *IEEE Trans. Ind. Electron.*, vol. 57, no. 4, pp. 1411–1419, Apr. 2010.

[28] B. Gao, J. Shao, and X. Yang, "A compound control strategy combining velocity compensation with ADRC of electro-hydraulic position servo control system," *ISA Trans.*, vol. 53, no. 6, pp. 1910–1918, 2014.

[29] L. L. Dong, "Application of active disturbance rejection control to micro-electro-mechanism system transducers," *Control Theory Appl.*, vol. 30, no. 12, pp. 1543–1552, 2013.

[30] A. Varatharajan, G. Pellegrino, E. Armando, and M. Hinkkanen, "Sensorless synchronous motor drives: A review of flux observer-based position estimation schemes using the projection vector framework," *IEEE Trans. Power Electron.*, vol. 36, no. 7, pp. 8171–8180, Jul. 2021, doi: 10.1109/TPEL.2020.3048922.

[31] J. Han, *Active Disturbance Rejection Control Technique-the Technique for Estimating and Compensating the Uncertainties*. Beijing, China: National Defense Industry Press, 2008, pp. 197–270.

[32] J. Han, "From PID to active disturbance rejection control," *IEEE Trans. Ind. Electron.*, vol. 56, no. 3, pp. 900–906, Mar. 2009.

[33] Y. H. Wang, Y. Yao, and K. M. Ma, "Analysis and application of Fal function filter," *Electric Mach. Control*, vol. 14, no. 11, pp. 88–91, 2018.

[34] H. K. Khalil and J. W. Grizzle, *Nonlinear Systems*. vol. 3. Upper Saddle River, NJ, USA:Prentice-Hall, 2002.

[35] S. Sastry, *Nonlinear Systems: Analysis, Stability, and Control*. vol. 10. New York, NY, USA: Springer Science and Business Media, 2013.

[36] M. Jansson, L. Harnefors, O. Wallmark, and M. Leksell, "Synchronization at startup and stable rotation reversal of sensorless nonsalient PMSM drives," *IEEE Trans. Ind. Electron.*, vol. 53, no. 2, pp. 379–387, Apr. 2006.

[37] J.-W. Choi and S.-K. Sul, "Inverter output voltage synthesis using novel dead time compensation," *IEEE Trans. Power Electron.*, vol. 11, no. 2, pp. 221–227, Mar. 1996.

[38] Z. Gao, "Active disturbance rejection control: A paradigm shift in feedback control system design," in *Proc. IEEE Amer. Control Conf.*, 2006, pp. 2399–2405.